The Astronomical Journal, 137:53–61, 2009 January doi:10.1088/0004-6256/137/1/53

STIS IMAGING OF THE HR 4796A CIRCUMSTELLAR DEBRIS RING

G. Schneider[1], A. J. Weinberger[2], E. E. Becklin[3], J. H. Debes[2], and B. A. Smith[4]
[1] Steward Observatory, The University of Arizona, 933 North Cherry Avenue, Tucson, AZ 85721, USA; gschneider@as.arizona.edu
[2] Department of Terrestrial Magnetism, Carnegie Institution of Washington, 5241 Broad Branch Road NW, Washington, DC 20015, USA; weinberger@dtm.ciw.edu, debes@dtm.ciw.edu
[3] Department of Physics and Astronomy, University of California at Los Angeles, Los Angeles, CA 90095, USA; becklin@astro.ucla.edu
[4] Institute for Astronomy, University of Hawaii, 2680 Woodlawn Drive, Honolulu, HI 96822, USA; basmith@ifa.hawaii.edu
Received 2008 July 21; accepted 2008 September 30; published 2008 December 2

ABSTRACT

We have obtained high spatial resolution imaging observations of the HR 4796A circumstellar debris dust ring using the broad optical response of the Hubble Space Telescope Imaging Spectrograph (STIS) in coronagraphic mode. We use our visual wavelength observations to improve upon the earlier measured geometrical parameters of the ring-like disk. Two significant flux density asymmetries are noted: (1) preferential forward scattering by the disk grains and (2) an azimuthal surface brightness anisotropy about the morphological minor axis of the disk with corresponding differential ansal brightness. We find the debris ring offset from the location of the star by $\sim$ 1.4 AU, a shift insufficient to explain the differing brightnesses of the northeast and southwest ansae simply by the $1/r^2$ dimmunition of starlight. The STIS data also better quantify the radial confinement of the starlight-scattering circumstellar debris, to a characteristic region less than 14 AU in photometric half-width, with a significantly steeper inner truncation than outward falloff in radial surface brightness. The inferred spatial distribution of the disk grains is consistent with the possibility of one or more unseen co-orbital planetary-mass perturbers, and the colors of the disk grains are consistent with a collisionally evolved population of debris, possibly including ices reddened by radiation exposure to the central star.

Key words: circumstellar matter – planetary systems: protoplanetary disks – stars: individual (HR 4796)

1. INTRODUCTION

HR 4796A (spectral type A0V) is the primary member of a binary system with a parallactic distance of 72.8 ± 1.7 pc in the newly revised *Hipparcos* catalog by van Leeuwen (2007). It is interesting to note that the distance has changed by more than 1σ from the determination of $67.1^{+3.6}_{-3.2}$ pc in the original *Hipparcos* catalog of Perryman et al. (1997). Its age, based upon that of its 7.″7 distant M2.5V coeval companion, is estimated at 8 ± 2 Myr (Stauffer et al. 1995).

The likely existence of a dusty debris disk around HR 4796A was inferred by Jura (1991) from its thermal infrared signature. He and collaborators (Jura et al. 1995) later suggested grain growth into larger particles at distances 40–200 AU from the central star. These predictions were borne out from 10 to 20 μm mid-IR observations by Koerner et al. (1998) and Jayawardhana et al. (1998) indicative of dust emission in a radial region bounded at 55–80 AU (now 60–87 AU with the revised distance). Coronagraphic observations by Schneider et al. (1999), with the *Hubble Space Telescope's* (*HST*) Near Infrared Camera and Multi-Object Spectrometer (NICMOS) at 1.1 and 1.6 μm (spatial resolutions 110 and 160 mas, respectively), directly imaged the dust, revealing a ring, 1.″05 (76 AU) in radius, with a width, as measured by its photometric FWHM, of $\lesssim$ 17 AU (now $\lesssim$ 18.5 AU). The NICMOS imagery also suggested that the northeast side of the disk was brighter than the southwest; a similar brightness asymmetry was seen in mid-IR observations by Telesco et al. (2000) and modeled by Wyatt et al. (1999). Preferential "forward" scattering by the dust grains was considered in models of the disk by Augereau et al. (1999).

We obtained high spatial ($\approx$ 70 mas) resolution optical images of the HR 4796A debris ring using the Space Telescope Imaging Spectrograph (STIS) in its coronagraphic imaging mode. From these data we examine in more detail the spatial distribution of the ring particles as inferred from spatially resolved imaging photometry along (and around) the ring. We confirm, and better quantify, the geometrical parameters defining the ring system and also measure two anisotropies in the photometric properties along the ring. Finally, we take this opportunity to discuss some of the details, intricacies, and methodologies employed in the reduction, processing, and analysis of *HST*/STIS coronagraphic imaging data. These will be the highest angular resolution visible-light images of the ring for some time. *HST*'s Advanced Camera for Surveys coronagraph provides a 0.″9 radius image plane mask, but has an effective inner working angle of $>$ 1.″2, limited mainly by point-spread function (PSF) subtraction residuals (e.g., Clampin et al. 2003). The HR 4796A disk is too small to be seen with that system.

2. OBSERVATIONS

A program of high spatial resolution imaging of the HR 4796A circumstellar debris ring was carried out using STIS in its coronagraphic imaging mode as part of *HST* general observer program 8624 (PI: Weinberger). With a foreknowledge of the ring geometry, an optimized imaging sequence was planned and executed using broadband optical coronagraphy (unfiltered spectral passband covering $\approx$ 2000–10500 Å with a pivot wavelength (λ_p) of 5752 Å, where λ_p is defined such that $F_\lambda = F_\nu c/\lambda_p^2$, and FWHM = 4330 Å).[5] Observations of HR 4796A were obtained at two epochs, 2001 February 17 and 2001 February 27, at spacecraft orientations differing by 16°, thereby rotating the debris ring orientation at the detector focal plane with respect to the STIS coronagraphic occulting wedge. At each epoch the orientation of the telescope was selected to simultaneously place the HR 4796A ring ansae at maximum angular distances from the STIS coronagraphic "A" wedge and from the stellar diffraction spikes (see Table 1).

[5] Pivot wavelength and FWHM values taken from Space Telescope Science Data Analysis System Synphot software.

Table 1
Observing Log for HR 4796A and HR 4748[a]

Visit	UT Date	Star	Orient[b]	UT Start	Exp. Time per Image (s)	No. of Images
11	2001 Feb 17	HR 4796A	282.058	17:38:16	6	18
A1	2001 Feb 17	HR 4748	283.272	18:04:51	4.2	18
12	2001 Feb 27	HR 4796A	298.057	05:53:18	6	18
A2	2001 Feb 27	HR 4748	281.420	07:16:01	4.2	18

Notes.
[a] Additional exposure-specific details may be obtained from the *HST* archive at http://archive.stsci.edu
[b] Position angle of the image *Y*-axis (east of north).

The STIS 50CCD aperture has an image scale of 50.70 mas pixel^{-1} and, unfiltered, provides a spatial resolution of $\approx$ 70 mas for stellar sources of $B - V$ color index 0.0 (such as HR 4796A and HR 4748); thus slightly undersampling the PSF. When combined, (in later processing) re-registered images at two field orientations provide better sampling of the PSF and also facilitate discriminating optical artifacts in the *HST*/STIS PSF from true circumstellar features.

Observations of a brighter star of nearly identical spectral type, HR 4748 (to serve as a PSF subtraction template) were obtained at each epoch. To minimize temporal variations in the *HST*/STIS PSF structure due to "breathing" of the telescope assembly (Schneider et al. 2001a) and small instabilities in the projected position of the STIS wedge onto the CCD focal plane, at each epoch, both HR 4796A and HR 4748 were observed during the same uninterrupted target visibility period. This entailed a small spacecraft slew of 1.°3 to HR 4748 following our HR 4796A observations (maintaining essentially the same spacecraft Sun angle for both pointings) with subsequent guide star and coronagraphic target acquisitions occurring without an intervening Earth occultation.

Onboard autonomous target acquisitions placed the stars on the mid-line of the standard coronagraphic "A" wedge where its tapered width narrows to 1.″0. Each target was then moved 7.″4 along the wedge mid-line to a location where the wedge is only 0.″63 wide. Target placement at this "nonstandard" location along the wedge was used to maximize the visible portion of the small HR 4796A ring. The target and PSF template star placements behind the occulting wedge were all within the nominal (27 mas, 3σ) combined STIS acquisition and pointing precision of the telescope.

The exposure sequences are given in Table 1 and summarized here. With the star occulted by the coronagraphic wedge, images were obtained with the unfiltered STIS CCD for total integration times of 108 s for HR 4796A and 75.6 s for HR 4748 at each epoch. Each individual image was 6 s (HR 4796A) or 4.2 s (HR 4748) in duration, and the 18 individual images were used for cosmic ray rejection and compensation. The individual exposures were planned to yield 72% of full-well depth at the edge of the wedge based upon ground-based photometry of the target stars and estimates of the anticipated instrumentally scattered and diffracted stellar light.

Except for the field orientations and integration times, the HR 4796A and HR 4748 exposures taken at the two epochs were executed in an identical manner, as detailed in Table 1. To reduce lost time in operational overheads, we employed a subarray readout mode of 80 rows centered on the target position. As a result, the known M-star companion to HR 4796A (Jura et al. 1993) does not appear in the images.

In addition to the coronagraphic images, target acquisition images of both stars (at both epochs) were obtained in the F25ND3 filter. Broadband images of these bright stars could not be obtained without saturating the detector.

3. DATA REDUCTION, PROCESSING, AND POST-PROCESSING

3.1. Calibration

The raw CCD frames were processed with the STSDAS *calstis* software task[6] using library flat field and dark current reference files from STScI's Calibration Database System[7] and nearly contemporaneous hot/bad pixel maps provided by the STIS Instrument Definition Team (IDT). At each epoch the individual images were combined for cosmic-ray rejection using the STSDAS *crreject* task and pixel values were converted to instrumental count rates (counts/second). Unrejected bad/hot pixels remaining in the combined count rate images were replaced by two-dimensional Gaussian weighted interpolation (with a weighting radius of 3 pixels) of neighboring good pixels. A residual frame-dependent fixed bias offset in the images was removed by subtracting a constant to force the background to zero far from the location of the star. The calibrated count rate images of HR 4796A and HR 4748 (re-normalized to the flux density of HR 4796A) at both epochs (and hence different field orientations) are shown in Figure 1. Though embedded in a wash of scattered and diffracted light from the core of the stellar PSF not rejected by the coronagraph, the HR 4796A ring is clearly visible in both HR 4796A frames (Figures 1(a) and 1(b)). The HR 4796A field (and hence the orientation of the ring) is rotated 16° between the two epochs, whereas the underlying structure of the *HST*+STIS PSF remains fixed on the detector. The rotational invariance of the stellar component of the PSF is apparent when comparing this to the contemporaneous observations of the reference star HR 4748, Figures 1(c) and 1(d).

3.2. PSF Subtraction

For each epoch, the calibrated HR 4748 images were simultaneously flux-scaled, astrometrically registered, and subtracted from their corresponding HR 4796A images with sub-pixel re-registration and resampling accomplished by sync-function apodized cubic convolution interpolation (Park & Schowengerdt 1983) as implemented in the NICMOS IDT's IDP3 software (Stobie et al. 2006). To make the best subtractions, we measured and iteratively minimized the PSF-subtracted diffraction spikes at radii of 15–30 pixels from the star (a region unaffected by disk flux but close to the radii at which the disk is brightest), as a

[6] Available from: http://www.stsci.edu/hst/stis/software/
[7] http://www.stsci.edu/hst/observatory/cdbs

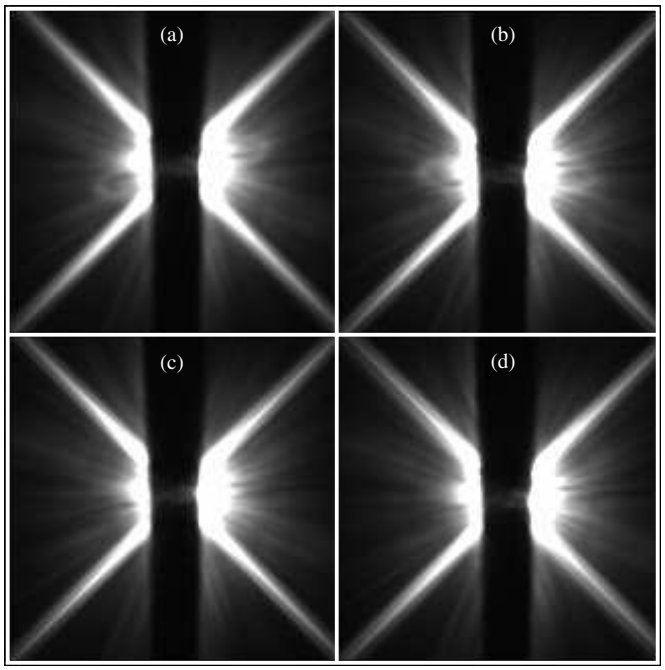

Figure 1. Panels (a) and (b) show HR 4796A in calibrated STIS 50CCD coronagraphic images from the two visits, and panels (c) and (d) show the PSF reference star HR 4748 in the corresponding visits. All panels are $3\farcs9 \times 3\farcs9$ and centered on the location of the star. The position angles of the +Y axis are 282.°06 east of north in (a) and 298.°06 in (b). The HR 4748 images have been scaled in brightness by a factor of 0.7 to match those of the paired contemporaneous observations of HR 4796A.

function of the position and flux scaling of the PSF template star. This was done separately for each visit-pair of target-template subtractions. Other means of optimizing the PSF subtractions, included flux scaling using the total energy along the diffraction spikes beyond a radius of 30 pixels while demanding that the median flux density of the background region to be statistically zero, give very similar results.

The best HR 4748:HR 4796A 50CCD band flux-density scaling was found to be 0.705. This is in statistical agreement with the F25ND3 ratio found from the target acquisition images. We estimate the uncertainty in this scaling as ± 0.002 by trying different minimization radii and widths. For the February 17 visit, the determined positional offsets of the PSF star to HR 4796 were $\Delta x = -0.360$ and $\Delta y = +0.388$ pixels. For the February 27 visit, the offsets were $\Delta x = -0.075$ and $\Delta y = 0.000$. We estimate the uncertainty in all target:PSF star position offsets as ± 0.020 pixels in both orthogonal directions from an examination of contours of χ^2 as a function of different positions. The relatively large ($\approx$ 18 mas) offsets on February 17 resulted from a target miscentering in the autonomous acquisition process that, unfortunately, introduced additional optical artifacts near the edge of the occulting wedge. The positions, scale lengths, and amplitudes of the optical artifacts due to miscentering under the wedge are different from those induced by "breathing" and are discussed in Section 3.3.

Our final image of the HR 4796A circumstellar ring is the average of the two visits; it is shown in Figure 2 and used for all further analysis in this paper. When averaging the two PSF-subtracted images, we masked out pixels unobserved due to the occulting wedge, pixels affected by the diffraction spikes, and pixels degraded by wedge–edge artifacts in the individual subtractions. The Visit 12 subtraction was registered to the position of the occulted star in the Visit 11 subtraction and rotated to the same celestial orientation.

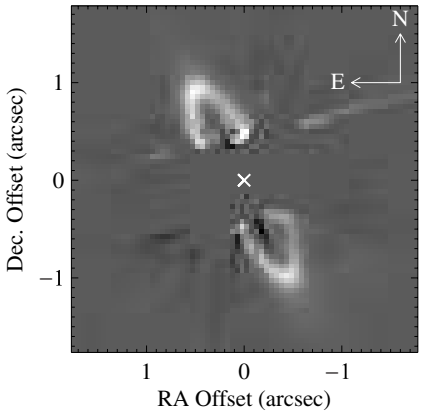

Figure 2. Final STIS 50CCD PSF-subtracted coronagraphic image of the HR 4796A circumstellar debris ring. The × marks the location of the star, as determined from the diffraction spikes in the unsubtracted image.

3.3. Artifacts in PSF-Subtracted Images

Residual low spatial frequency systematic artifacts remain in the combined image. These artifacts arise, primarily, from the interaction of two effects: different centerings under the wedge of HR 4796A and the reference PSF and a slight defocus (breathing excursion) in the Visit 12 PSF relative to HR 4796A image taken in the same visibility period. They may be thought of as comprised of several "features." Most obvious among them are the radial "spokes." We also see a radial modulation of the background intensities, and a "hemispheric" bias in that modulation due to decentering. As a result, it is not possible to simultaneously obtain zero nulling of the backgrounds at all radii with the subtraction method described in Section 3.2. The PSF-subtracted "input" images employed global nulling and minimization in their creation, but they do not show "optimal" subtraction in all radial zones.

The specific spatial nature of these residuals is complex. Building a multiparameter (or multidimensional) model in the hopes of achieving truly global background minimization is likely infeasible because many instrumental effects, such as wavelength- and position-dependent wedge–edge scattering that remain uncharacterized. We accept that a global, fully optimized PSF-subtracted image may not be achievable.

The northeast side of the ring is less affected by residual diffraction and instrumental scattering artifacts than the southwest side of the ring. The appearance of the artifacts in the PSF-subtracted images may be better understood by examining paired subtractions of the individual HR 4748 PSFs (Figure 3). Because the star positions in the two visits were offset in X with respect to the wedge centerline, one edge of the wedge appears bright, and the other dark after registration and subtraction. The stellar positions were also offset in Y (along the wedge) changing, in detail, the scattered-light profile from the edge of the wedge. Additionally, a very small focus change occurred causing the asymmetrical appearance of the $+45^\circ$ and -45° diffraction spike residuals. Despite these nonrepeatabilities, the registration process mimics the minimization of the radial streaks as was done for the HR 4796A PSF subtractions.

Figure 3 illustrates the nature and spatial distribution of the subtraction residuals within $1''$ of the star before combination into the final image. Small differences between the individual PSF-subtracted images are seen. Also shown are the azimuthally changing influences of image artifacts within each PSF-subtracted image. For example, due to the Visit A1

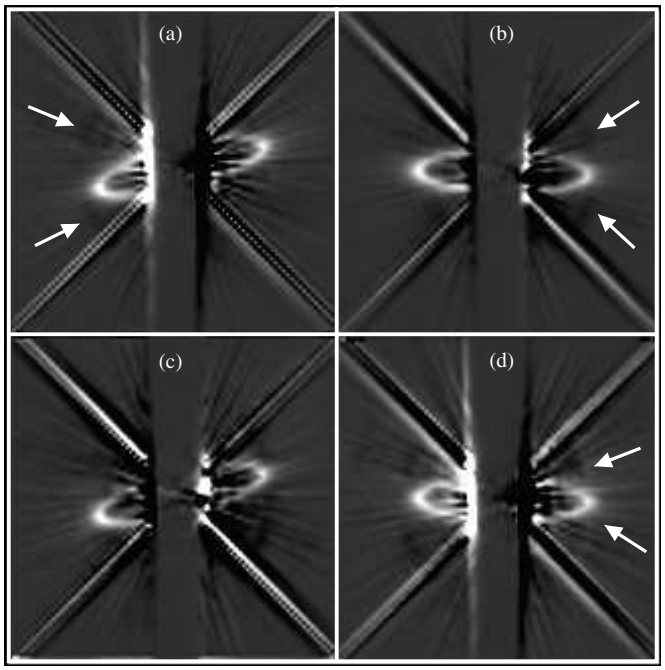

Figure 3. PSF-subtracted images of HR 4796A after PSF flux scaling and registering. The four panels show different target/PSF combinations. HR 4796A images from Visit 11 are at the left (a, c) and Visit 12 at the right (b, d). The top row shows subtractions using the contemporaneous observations of HR 4748 (11 − A1 for (a) and 12 − A2 for (b), and the bottom row shows the opposite pairs (11 − A2 for (c) and 12 − A1 for (d)). The image scales and orientations are the same as in Figure 1. The arrows indicate some of the subtraction residuals discussed in Section 3.3. In panel (a), the arrows point to the negative zone near the northeast ansa. In panel (b), they point to the negative residuals near the SW ansa. In panel (d), they show the positive residuals to the SW.

decentering of the HR 4748 reference PSF with respect to the mid-line of the wedge, the resulting low-amplitude, large spatial scale, negative residuals in the PSF subtraction are less pronounced on either side of the NE ansa; i.e., locally, this is a "cleaner" PSF subtraction then around the SW ansa.

The artifacts in individual subtractions are partially self-canceling in weighted average combination, but unfortunately not completely so. Note in Figure 3 that the negative-going residuals at radii just at and marginally beyond the southwest ansa are of larger amplitude in the subtractions using the Visit A2 reference PSF (Figures 3(b) and 3(c)), and more noticeable in Figure 3(b) because of the lower amplitude of the radial spokes as the HR 4796A-to-HR 4748 relative centering was very precise. A dark (negative) zone is seen abutting the northeast ansa in the subtractions of the Visit A1 PSF (Figures 3(a) and 3(d)), where the reference PSF star was significantly offset from the wedge center. Finally, note that there is a zone of positive residuals seen in Figure 3(d) subtraction to the SW just outside of the radius of the negative zone.

4. RESULTS

4.1. Ring Geometry

We exploit the high spatial resolution of the STIS data to improve upon the initial determination of the geometrical parameters of the ring derived from the NICMOS scattered-light images by Schneider et al. (1999). By ring geometry we mean: (a) the location of its center (determined separately from the position of the star), (b) its ellipticity (apparent eccentricity; we interpret the apparent ellipticity as evidence for a disk which is intrinsically circular (or nearly so) and inclined to our line of sight and use it to calculate an inclination), (c) the major axis length that corresponds to the ridge of maximum surface brightness in a deprojected ellipse, and (d) the major axis celestial position angle of the apparent ellipse.

Table 2
Ring Geometry

Position Angle of the Major Axis	$27\overset{\circ}{.}01 \pm 0\overset{\circ}{.}16$
Major:Minor Axis Length Ratio	4.10 ± 0.05
Implied Inclination	$75\overset{\circ}{.}88 \pm 0\overset{\circ}{.}16$
Ansal Separation (Photocentric Peaks)	41.563 ± 0.088 pixels
	$2\overset{''}{.}107 \pm 0\overset{''}{.}0045$
Major Axis (Best-Fit Ellipse)	41.698 ± 0.108 pixels
	$2\overset{''}{.}114 \pm 0\overset{''}{.}0055$
Henyey–Greenstein g	0.16 ± 0.06
Ansal Asymmetry Factor	0.74 ± 0.07

We determined the geometry of the ring in two ways. First, we fit ellipses to the ring isophotes at the 25%, 50%, 75% (interior and exterior to the peak), and 100% flux density levels normalized at each azimuth (in 5° deprojected increments; see Figure 4) to the maximum intensity at each position angle in each azimuthal bin. In doing so we exclude data behind and immediately adjacent to the coronagraphic wedge and diffraction spikes. All of the geometrical parameters, except the semimajor, axis were determined from the mean of the seven isophotal fits; the semimajor axis length (which corresponds to a deprojected radius of maximum surface brightness) was determined from the 100% isophotal contour alone (shown in Figure 5). The seven fit ellipses were concentric to within 6 mas.

Second, we built a model of the disk assuming an elliptical ring with a surface brightness profile across the ring described by a Gaussian. The model geometry is defined by five free parameters, corresponding to those independently measured as described above: ellipse center (x and y), semimajor axis length and orientation, and inclination. The disk model also includes two other free parameters: the ring Gaussian width and overall intensity normalization (i.e., a scale factor to match the total disk flux density). For this purpose, we modeled the forward scattering with a Henyey–Greenstein prescription (see Section 4.3). Finally, we modeled the ansal asymmetry as a smooth sine function peaked along the major axis at the northeast ansa and decreasing to the southwest side with an amplitude equal to the photometrically measured asymmetry (see Section 4.4). The model free parameters were iteratively adjusted to fit the observational data with χ^2 minimization.

The geometrical parameters determined by the two independent methods agree very well, and the averages from the two methods (and their resulting uncertainties) are presented in Table 2. In Figure 5, we show the best-fit ellipse (in black) defined by the systemic parameters detailed in Table 2 overlaid on 3.2% photometric intensity contours (see scale bar in Figure 4).

4.2. Stellocentric Offset

The stars themselves are hidden under the coronagraphic wedge during the observations, so their positions cannot be measured directly. Hence, we determined the location of HR 4796A in each visit by using the unocculted portions of the stellar diffraction spikes beyond the coronagraphic wedge. We assume the diffraction spikes are centered on the star. At every detector column, a slice was made through the spikes, and the center of the spike was found by fitting a Gaussian profile

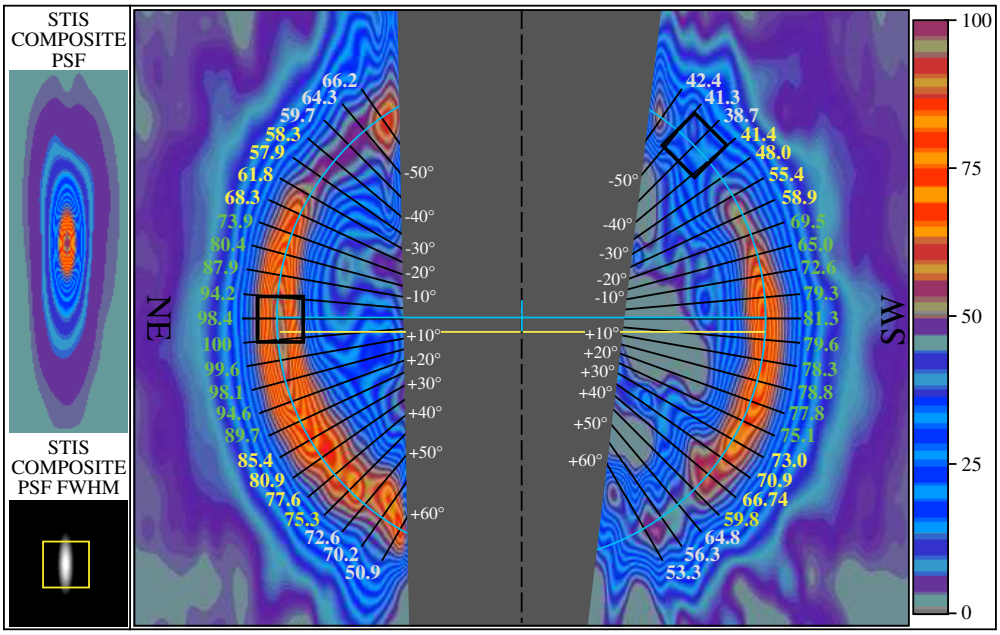

Figure 4. Deprojected image of the disk, with flux conservation, showing flux isophotes. The color bar shows 3.2% intensity isophotes switching from orange to blue at 50% of the peak intensity. We fit concentric circles to seven ring isophotes at the 25%, 50%, 75%, and 100% flux density levels normalized at each azimuth to the maximum intensity at each position angle in each azimuthal bin. Azimuthal samples were made at 5° deprojected increments as marked on the interior of the image. Photometry for these samples was done in apertures fully enclosing the projected FWHM of the STIS PSF, as shown in the bold black squares, which are rotated to maintain a fixed inner and outer distance from the ring center. The numbers around the periphery of the disk image give the percentage of flux relative to the bright ansal peak at each fit point along the 100% contour. The light blue circle shows the best fit at the 100% contour. The horizontal blue line shows the ellipse major axis. The yellow line connects the ansae and therefore shows the offset of the ellipse due to forward scattering. Also shown at left are what the STIS PSF looks like when deprojected, (top) on a stretch that shows all of its details, and (bottom) the same PSF clipped at the FWHM to show only the core shape. The yellow square on the lower PSF shows the size of the photometric extraction aperture.

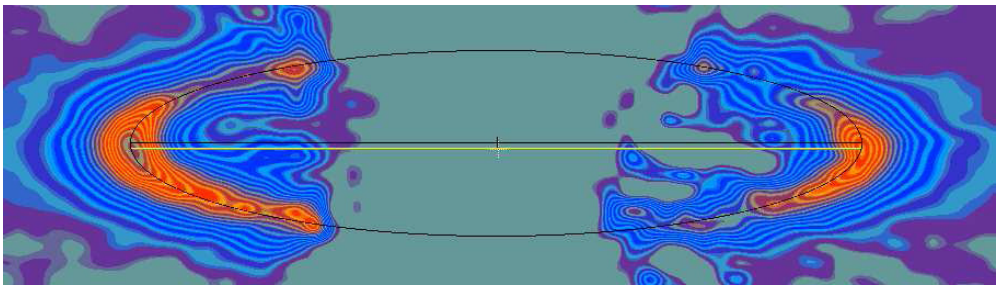

Figure 5. Best-fit ellipse (in black), determined from the contours as described in the text, shown overplotted on the HR 4796 image. The yellow line connects the ansae, and is parallel to the major axis of the ellipse to within the uncertainties. The vertical tick marks the center of the BFE.

to the slice. A least-squares fit was made to the coordinates of the two orthogonal spikes, with the intersection defining the location of the star. The diffraction spikes are easily traced from a distance of 9 pixels (0.″46) from the star (beyond the edge of the occulting wedge) to 44 pixels (2.″23) at the edge of subarray used to read out the image. The formal uncertainty on the fit location of the center is 0.08 pixels in each coordinate from propagating the uncertainty in the two least-squares fits.

The wedge-occulted positions of HR 4796A resulting from the independent target acquisitions in Visits 11 and 12, as determined from the above diffraction spike fitting method, were found to be (306.41, 41.28) ± (0.09, 0.06) pixels and (306.09, 40.01) ± (0.07, 0.08), respectively, in the STIS CCD science instrument aperture frame (SIAF). The inferred target positioning offset between the two visits is therefore (+0.32, +1.27) ± (0.11, 0.10) pixels. This offset was independently checked using the diffraction spike noise-minimization iterative-subtraction method described in Section 3.2 applied to the two HR 4796A visits; from which a position offset of (+0.26, +1.30) pixels was found (i.e., within 1σ of the offset determined directly from diffraction spike fitting).

We compare the position of the star to the geometrical center of the ring ellipse to investigate the possibility of a stellocentric offset such as seen in the case of the Fomalhaut debris ring as discussed by Kalas et al. (2005)[8].

We found the distance between the two ring ansae and the star by placing the stellar center at the middle of a pixel and rotating the final image about the center so the major axis was horizontal. We took a 1 pixel slice along the major axis and fit the locations of the ansae in this slice with Gaussians. We find that the northeast ansa is 20.522 ± 0.041 pixels (1.″040 ± 0.″002) and the southwest ansa is 21.287 ± 0.069 pixels (1.″079 ± 0.″003) from the stellar center, as shown in Figure 6. These uncertainties are the formal uncertainties from the Gaussian fit and do not include the uncertainty in the center found above. To make the

[8] Kalas et al. (2008) report the discovery of an estimated 3 Jupiter mass planet orbiting interior to the Fomalhaut debris ring that may be responsible for its stellocentric offset.

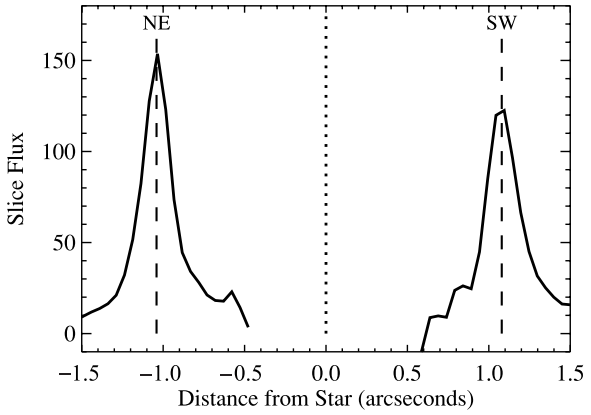

Figure 6. A 1 pixel slice along the major axis of the disk shows the locations of the northeast and southwest ansae at distances of 1.″040 and 1.″079 from the star, respectively. These locations are shown with the vertical dashed lines. The stellar location at zero is marked with a dotted line. The point halfway between the ansae, i.e., the ring center, appears shifted 19 ± 6 mas away from northeast ansa, where this uncertainty includes contributions both from fitting the locations of the ansae and determining the stellar center. At the distance to HR 4796 of 72.8 pc, this is a ring offset of 1.4 ± 0.4 AU.

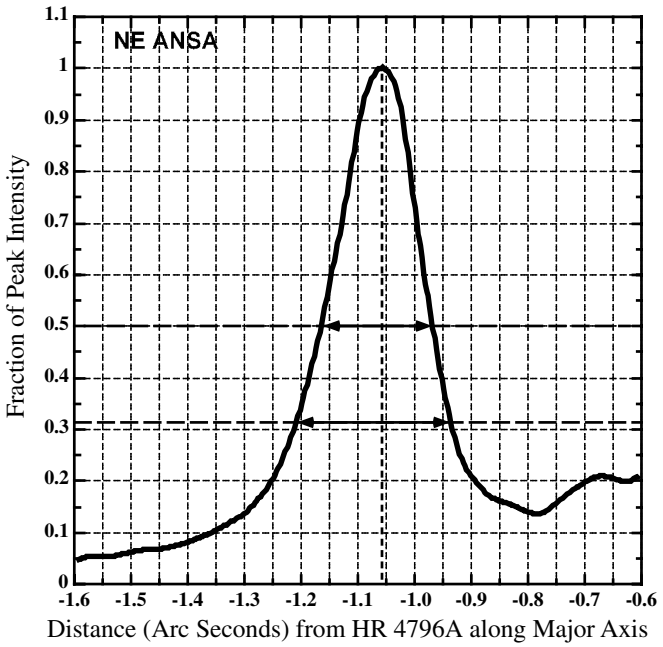

Figure 7. Characteristic width of the HR 4796A ring defined from a cross-sectional profile through the northeast ring ansa along the major axis of the BFE. The arrows show the cross-sectional profile's exterior and interior half-widths at half-intensity maximum and $1 - 1/e$ of the maximum. The distance along the major axis is measured from the center of the best-fit ellipse.

ansae equidistant implies a ring center shifted away from the northeast ansa by 0.38 ± 0.12 pixels $= 0.''019 \pm 0.''006$. Because the portion of the ring along its minor axis is obscured by the coronagraphic wedge, we cannot robustly set a limit on a star–ring offset in this direction.

4.3. Width of the Dust Ring

HR 4796A disk grains are radially confined to a narrow annular zone circumscribing the star. Radially across the northeast (brighter) ansa we measure a 1 pixel wide FWHM of the surface brightness profile as 0.″197, but the brightness fall-off is somewhat steeper interior to the ring ansa then outward from it (see Figure 7), indicating a sharper interior cut-off than the outer truncation. In particular, the measured HWHM interior to the northeast ansa is 0.″089 whereas exterior to the ansa it is 0.″108. An azimuthally averaged radial profile, extending in sectors $\pm 15^\circ$ in elliptical coordinates derived from the geometrical eccentricity of the ring, about the ring ansae, is best fit to a broader Gaussian with a FWHM of 0.″222. Taking individual 1 pixel wide profiles (in 5° deprojected increments) around the ring, the FWHM of the radial surface brightness profiles is seen to be at a minimum through the ansae, and increases in radial profiles closer to the ring minor axis. These effects are opposite of what one would expect for a perfectly flat disk and likely indicates scattering from dust above the mid-plane of the disk.

We characterize the width of the annular region confining most of the starlight-scattering dust by the intrinsic FWHM of the ring at the brighter ansa, which as measured is instrumentally broadened by the STIS 50CCD (unfiltered) PSF. Subtracting the FWHM of the STIS 50CCD PSF (0.″070) in quadrature from the observationally measured width, we find the intrinsic characteristic ring width to be FWHM 0.″184 (13.4 ± 0.8 AU, at the revised stellar parallax, or 8.7% of the ring diameter) with corresponding HWHM[inner] $=$ 0.″082 and HWHM[outer] $=$ 0.″102. This is consistent with the upper limit set by Schneider et al. (1999) from the lower spatial resolution NICMOS images.

4.4. Forward Scattering

For an inclined disk, the side centered on scattering phase angle 0° is seen primarily in forward scattered starlight while the other half, centered on scattering phase angle 180°, is seen primarily in light that is backscattered. The HR 4796A scattered-light disk is clearly brighter on the east side (both north and south of the minor axis) than on the west side. To determine if the ring dust displays significant azimuthally non-isotropic scattering, we measured and ratioed, the total flux density in symmetrically placed sectors within the four readily visible quadrants of the disk—between 5° and 20° from the major axis, and within 0.″8–1.″5 from the star.

We characterize this asymmetry in terms of a Henyey–Greenstein phase function parameter, g, at the best-fit inclination of 14.°1 from edge-on. The variable g represents a measure of the "front-to-back" light-scattering asymmetry of the dust, where $g = 0$ represents a completely isotropic phase function and $g = 1$ represents purely forward scattering. The scattering angle, θ, between an incoming ray of light and the line of sight for an observer was calculated following the formalism in the Appendix A of McCabe et al. (2002). Making a Henyey–Greenstein model and integrating over the observed scattering angles within each of the four photometric apertures described above, using different g values, we find a best fit for the measured inter-sector flux density ratios with $g = 0.16 \pm 0.06$, or evidence for forward scattering at the 2.7σ level of confidence.

We also measured the ansa-to-ansa orientation angle, from the centroid of one ansa to the other, as $26.^\circ6 \pm 0.^\circ5$. The difference between this orientation and the P.A. of the best-fit disk ellipse (27.01 ± 0.16; Table 2) is $0.^\circ4 \pm 0.^\circ5$. That these position angles agree is another indication that it is forward scattering that shifts the locations of the ansae away from the disk semimajor axis (see the yellow line in Figure 4).

4.5. Ansal Asymmetry

The northeast side of the disk (flanking the brighter ansa) appears brighter than the southwest side. To measure this asymmetry, we took the total flux density in the northeast and

southwest "lobes," within ±20° of the major axis, and measured their ratios in those sectors between 0.″8 and 1.″5 from the star (using the same background annulus as for the total disk photometry). The southwest side is 0.74 ± 0.07 as bright as the northeast side.

4.6. Photometry

Determining the flux density of the unobscured portion of the HR 4796A ring is most affected by two sources of systematic uncertainties in the measurements. Intrinsically, the uncertainty in the brightness of the ring in the STIS 50CCD instrumental system is dominated by optical artifacts arising from the imperfect PSF subtractions (i.e., not by photon statistics or other "random" noise sources). Extrinsically, effecting a photometric transfer from the instrumental system to a standard photometric system (e.g., Johnson/Vega) is difficult because of the extreme breadth of the 50CCD bandpass (FWHM = 75% of the pivot wavelength) and because the intrinsic SED/color of the disk within that band is unknown. We address these systematic errors separately.

We measure the 50CCD bandpass disk flux density in an elliptical aperture with the major:minor axis ratio and position angle as we determined for the disk, and an inner semimajor axis of 0.″8 and an outer semimajor axis of 1.″5. Inside 0.″8, pixel-to-pixel fluctuations dominate the flux density measures on pixel size scales, and outside 1.″5, light from the disk is less than 5%–10% of the peak surface brightness. Since only part of the disk was visible, we restricted our aperture to be within 20° of either side of each ansa. We used an elliptical annulus between 2.″09 and 2.″50 with the same azimuthal coverage to determine the background level of the image.

To estimate the systematic uncertainties introduced by PSF subtraction, we create a grid of PSF-subtracted images in which we (a) offset the PSF template relative to the best-determined position by 1σ of the uncertainties in the X and Y (SIAF) co-aligned position determinations and (b) rescale the intensity of the PSF template by 1σ from the best-determined target:template scaling ratio. We use the resulting standard deviation of the pixels in our photometric aperture, over all the points in this grid, as an estimate of the per-pixel photometric systematic uncertainty. We then apply this uncertainty to each pixel in our photometric apertures.

To convert from raw instrumental units of counts s^{-1} $pixel^{-1}$ to per-pixel flux density in physical units of mJy under the STIS 50CCD (unfiltered) passband, we adopt the instrumental sensitivity and photometric zero point from version 7.0 (2003 October) of the STIS Instrument Handbook for a spectrally flat source: AB magnitude 26.386 = 1 count s^{-1} (with an instrumental gain of 4.096 e^- $count^{-1}$ as used for all our observations), with a zero-point magnitude of 3631 Jy.

The 50CCD band flux density of the visible portion of the disk unocculted by the coronagraphic wedge and within the photometric measurement aperture is then 5.47 ± 0.24 mJy (with the presumption of a flat spectrum). While this is likely to be very close to correct for an A0V ($B - V = 0.0$) star, such as HR 4796A, the spectral reflectance of the disk grains in the broad optical to near-IR is red (Debes et al. 2008) and will bias the flux density transformations into standard photometric bands. We use the *calcphot* task in the STSDAS synphot synthetic photometry package (which provides a high-fidelity model of the STIS instrumental response) to estimate this photometric uncertainty. For disk grains as red as $B - V = +0.60$, the V-band brightness of the disk (transformed from the broad 50CCD passband) would be 0.047 mag brighter than for grains with a spectrally neutral ($B - V = 0.0$) reflectance; i.e., a 5% error in the absolute photometric calibration due to an uncertainty of this amount in the $B - V$ color of the circumstellar debris.

We compensate for the flux density originating from the unsampled portion of the disk using the geometrical parameters in Table 2. We do this by building a model of the disk that includes: (a) a Henyey–Greenstein phase function with the g value measured in Section 4.4, (b) an ansal asymmetry characterized by a sine dependence and a maximum excursion given in Section 4.5, (c) a width from the measured radial profile given in Section 4.1, and (d) size from the measurements described in Section 4.1. This model yields a total disk flux density 1.71 times greater than in the measured region alone; if the entire spatial region of the disk could have been measured, we would therefore expect a 50CCD band total disk flux density of 9.4 ± 0.8 mJy.

5. DISCUSSION

The ∼70 mas per resolution element STIS observation of the HR 4796A debris disk better elucidates the morphology and geometry of the circumstellar ring than the longer wavelength NICMOS observations. Most, if not all, of the "clumpiness" seen in the Schneider et al. (1999) near-IR images of the ring was then suggested as arising from optical artifacts in the NICMOS PSF subtractions, rather than intrinsic to the dust distribution, and that indeed appears to be the case.

5.1. Ansal Asymmetry

A hemispheric brightness asymmetry was suggested in both the NICMOS F160W and F110W (1.6 and 1.1 μm) bands at the 10%–15% level as noted by Schneider et al. (2001b). A similar brightness asymmetry was seen in the mid-IR and discussed by Telesco et al. (2000). This work shows the asymmetry in the broadband optical to be about 25%.

One model for the mid-IR asymmetry was "pericenter glow," a forced eccentricity of the disk that resulted in one side's grains lying closer to the star and therefore being heated to a higher temperature (Wyatt et al. 1999). To explain the mid-IR observations of Telesco et al. (2000), required a radial offset asymmetry, $(R_{SW} - R_{NE})/R_{mean} = 6.4\%$ (Wyatt et al. 1999).

We measure the offset between the center of the ring and the star along the ring major axis to be 19 ± 6 mas or 1.4 AU (Figure 6), for a radial offset asymmetry of 3.7%. Of course, the true displacement may include a component toward or away from us. In that case, what we interpret as forward scattering could be partially due to the east side of the disk being closer to the star than the west side. The magnitude of such a shift is limited by the small asymmetry we measure.

In any case, the offset along the major axis of 3.7% causes a brightness asymmetry, just due to the r^{-2} dependence of the stellar brightness, of 14%, which is approximately half of the observed difference in the ansal brightnesses.

This asymmetry could also be due to an azimuthally inhomogeneous population of disk grains, or arise from a non-uniform spatial distribution of an intrinsically homogeneous population. Given orbital periods of ∼350 yr for ring particles at the characteristic radius of 76 AU, and an age of the star of ∼8 Myr, one would expect the grains to be well mixed rather than azimuthally segregated populations of grains with different scattering efficiencies. We suggest the possibility that the

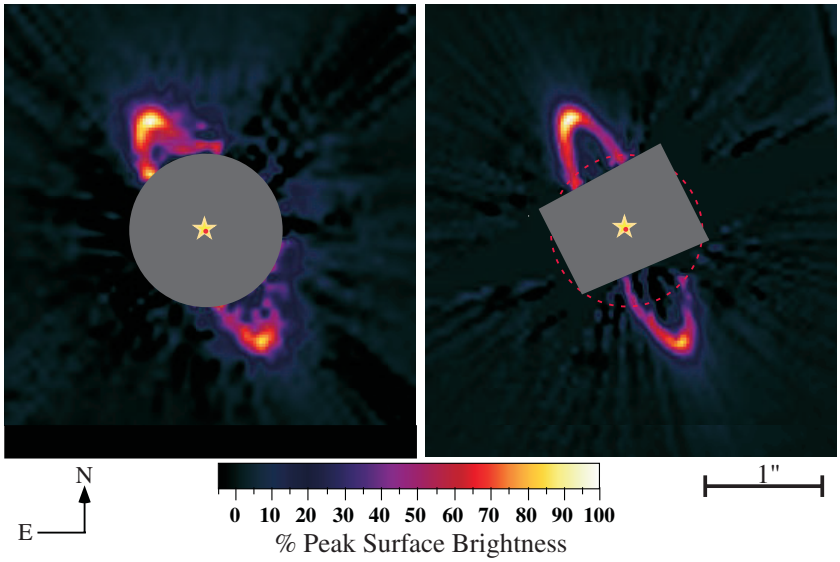

Figure 8. Comparison of the NICMOS image of HR 4796A from Schneider et al. (1999) with the image from this work. For purposes of display and to highlight the morphology, the STIS image has been resampled 2 times (as was the NICMOS image) and low-level background modulation from PSF subtraction at radii $< 1''$ has been estimated by Krieg interpolation and removed. The red dot marks the center of the ring while the yellow star marks the location of the star. Both images show a decrement in ring brightness at P.A. $\sim 230°$.

hemispheric variation in surface brightness might arise, at least in part, from a dynamical redistribution of the grains, through perturbations or resonant interactions with co-orbital bodies, leading to azimuthally confined regions of enhanced particle densities. Wyatt et al. (1999) describe the effect of forced eccentricities from the companion, which might be sufficient to explain a portion of the asymmetry. Kuchner & Holman (2003), e.g., describe more generally how planets can concentrate dust at resonances.

5.2. An Intra-Ring "Gap"?

We note the appearance of a correlated decrement in the ring brightness at a position angle (eastward from north) of $230° \pm 10°$ in both the NICMOS F110W and STIS 50CCD images (Figure 8). The statistical significance of this is not strong in the individual images; however, the correlation of this "feature" in the two images, taken at significantly different field orientations, wavelengths (PSF subtraction artifacts spatially scale with wavelength), and instruments, is intriguing and suggests there might be a gap in the distribution of ring particles at that azimuth. This, perhaps, is further evidence (albeit not very strong on its own) of azimuthal sculpting of the grains by gravitational perturbation by one or more undetected bodies of planetary mass. This region is nearly opposite the bright ansa, and is in the direction of the companion M-star that sits $7\farcs7$ away at a P.A. $= 225\fdg4$.

5.3. "Confinement" of the Disk Particles

The central "hole," seen to an inner radius of $\sim 0\farcs5$ (35 AU) in the 50CCD images is essentially cleared of circumstellar material which would otherwise scatter starlight. A similar central clearing is apparent (as implied from the radial inward brightness fall-off) in the Schneider et al. (1999) 1.1 and 1.6 μm NICMOS images. Additionally, Telesco et al. (2000) find a mid-IR optical depth in the central zone of less than 3% from 10.8 and 18.2 μm imaging. The disk's emitting regions are spatially coincident with the scattered light seen in the optical and near-IR.

Small particles may be cleared by radiation pressure and Poynting–Robertson drag acting on timescales much shorter than the estimated $\sim$8 Myr age of HR 4796A if the dust were not replenished and/or confined. The number of grains in the ring, as inferred from the mid-IR observations, implies that the dust in the ring should be collisionally dominated. It is likely that mutual collisions disintegrate large grains until they are small enough to be removed by radiation pressure. Then, the absence of dust interior to the starlight-scattering ring indicates a corresponding absence of large bodies located there (Kenyon et al. 1999).

The outer "truncation" of the disk might be dynamically aided by HR 4796B, the M-star companion to HR 4796A noted by Jura et al. (1995), though it is at a projected (minimum) distance of $\sim$500 AU. Dynamical models of the ring must also reproduce the relatively sharp inner, and slightly less steep outer ring boundaries. Such tight bounding might be manifested by the "shepherding" of the ring particles by co-orbital bodies (Goldreich & Tremaine 1979), loosely analogous, for example, to structures seen in the Saturnian rings, but here on solar system size scales.

5.4. Color (Spectral Reflectivity) of the Grains

We have found the HR 4796A disk grains to be significantly red at optical to the near-IR wavelengths; this result is discussed in some depth in a companion paper (Debes et al. 2008). Intrinsically red grains are consistent with a collisionally evolved population of particles where the characteristic particle size is larger than the wavelengths of the observations, as opposed to neutral or blue grains which would be more typical of a primordial population of ISM grains.

HR 4796A's disk is not the only one to display such red colors. The more substantial disk around HD 100546 also shows red optical scattering (Ardila et al. 2007), as do portions of the similarly thin β Pictoris disk (Golimowski et al. 2006). Perhaps the reddening mechanism (e.g., Andronico et al. 1987) is common to both our outer solar system and the cool portions of younger disks around more luminous stars.

We gratefully acknowledge contributions from members of the STIS IDT leading to a better understanding of some of the performance characteristics of the instrument, and in particular Phil Plait for assisting with some of the nuances of STIS data calibration, and Carol Grady and Randy Kimball in regard to temporal stability and pointing precision issues. We also wish to thank other members of the NICMOS IDT for their suggestions and comments during the investigatory phases of this study, and specifically to Marcia Rieke for establishing the absolute photometric calibration of NICMOS, and Elizabeth Stobie for implementing significant improvements to the IDP3 software in support of this study. This work is based on observations with the NASA/ESA *HST*, obtained at the Space Telescope Science Institute, which is operated by AURA, Inc. under NASA contract NAS2-6555 and supported by NASA grants NAG5-3042 and GO 8624 and 10177.

REFERENCES

Andronico, G., Baratta, G. A., Spinella, F., & Strazzulla, G. 1987, A&A, 184, 333
Ardila, D. R., Golimowski, D. A., Krist, J. E., Clampin, M., Ford, H. C., & Illingworth, G. D. 2007, ApJ, 665, 512
Augereau, J. C., Lagrange, A. M., Mouillet, D., Papaloizou, J. C. B., & Grorod, P. A. 1999, A&A, 348, 557
Clampin, M., et al. 2003, AJ, 126, 385
Debes, J. H., Weinberger, A. J., & Schneider, G. 2008, ApJ, 673, L191
Goldreich, P., & Tremaine, S. 1979, Nature, 277, 97
Golimowski, D. A., et al. 2006, AJ, 131, 3109
Jayawardhana, R., Fisher, S., Hartmann, L., Telesco, C., Pina, R., & Fazio, G. 1998, ApJ, 503, L79
Jura, M. 1991, ApJ, 383, L79
Jura, M., Ghez, A. M., White, R. J., McCarthy, D. W., Smith, R. C., & Martin, P. G. 1995, ApJ, 445, 451
Jura, M., Zuckerman, B., Becklin, E. E., & Smith, R. C. 1993, ApJ, 418, L37
Kalas, P., et al. 2008, arXiv:0811.1994v2
Kalas, P., Graham, J. R., & Clampin, M. 2005, Nature, 435, 1067
Kenyon, S. J., Wood, K., Whitney, B. A., & Wolff, M. J. 1999, ApJ, 524, L119
Koerner, D. W., Ressler, M. E., Werner, M. W., & Backman, D. E. 1998, ApJ, 503, L83
Kuchner, M. J., & Holman, M. J. 2003, ApJ, 588, 1110
McCabe, C., Duchêne, G., & Ghez, A. M. 2002, ApJ, 575, 974
Park, S., & Schowengerdt, R. 1983, Comput. Vis. Graph. Image Process., 23, 256
Perryman, M. A. C., et al. 1997, A&A, 323, L49
Schneider, G., Becklin, E. E., Smith, B. A., Weinberger, A. J., Silverstone, M., & Hines, D. C. 2001a, AJ, 121, 525
Schneider, G. NICMOS/EONS & GTO/8624 Teams 2001b, in ASP Conf. Ser. 244, Young Stars Near Earth: Progress and Prospects, ed. R. Jayawardhana & T. Green (San Francisco, CA: ASP), 203
Schneider, G., et al. 1999, ApJ, 513, L127
Stauffer, J. R., Hartmann, L. W., & Barrado y Navascues, D. 1995, ApJ, 454, 910
Stobie, E., et al. 2006, in ASP Conf. Ser. 351, Astronomical Data Analysis Software and Systems XV, ed. C. Gabriel, et al. (San Francisco, CA: ASP), 540
Telesco, C. M., et al. 2000, ApJ, 530, 329
van Leeuwen, F. 2007, Hipparcos, the New Reduction of the Raw Data (New York: Springer)
Wyatt, M. C., Dermott, S. F., Telesco, C. M., Fisher, R. S., Grogan, K., Holmes, E. K., & Piña, R. K. 1999, ApJ, 527, 918